ELSEVIER

Contents lists available at ScienceDirect

# Geochimica et Cosmochimica Acta

journal homepage: www.elsevier.com/locate/gca





# Nitrogen partitioning between silicate phases and aqueous fluid depends on concentration

Colin R.M. Jackson a, Elizabeth Cottrell b

- a Department of Earth and Environmental Sciences, Tulane University, United States
- <sup>b</sup> Department of Mineral Sciences, National Museum of Natural History, Smithsonian Institution, United States

#### ARTICLEINFO

Associate editor: Ralf Halama

Keywords: Nitrogen Partitioning Silicate Fluid

#### ABSTRACT

The distribution of nitrogen in geologic systems is modulated by its partitioning between silicate (mineral and melt) and fluid phases. Under geologically applicable oxygen fugacity, pressure, and temperatures, nitrogen can be multiply-speciated, with N<sub>2</sub> coexisting with reduced nitride (N<sup>-3</sup>) species. Non-polar, neutral species, including N<sub>2</sub>, tend to concentrate in fluids, while charged nitride species have a greater propensity to concentrate in silicate phases. The stoichiometry of converting  $N_2$  to single N atom nitride species implies that nitrogen speciation may depend on its concentration, and this leads to the hypothesis that the partitioning of nitrogen between silicate and fluid phases also depends on concentration, potentially biasing prior experimental work in doped systems and influencing the behavior of nitrogen in geologic systems. To test this hypothesis, we have completed a series high pressure (~1.75 GPa, 800 °C) experiments that react minerals, melts, and fluids with variable nitrogen concentrations (3.1-17.1 wt% N). Our results imply order-of-magnitude-scale increases in mineral/melt and melt/fluid partitioning as nitrogen concentrations decrease within natural ranges. For example, decreasing the N concentration from 2500 to 2 ppm increases predicted  $D^N_{melt/fluid}$  values by over an order of magnitude at constant PT conditions. This means that loss of nitrogen from a degassing magma or dehydrating slab is a self-limiting process that becomes increasingly inefficient as nitrogen concentration falls. Despite this, nitrogen remains highly concentrated in the atmosphere, which receives N from fluids exsolved from slabs and magmas. To maintain a nitrogen-rich atmosphere we therefore suggest that warm and oxidizing conditions have prevailed over subduction zones because warm slabs dehydrate under lower pressures where nitrogen is more easily partitioned into fluids, and oxidizing conditions also promote nitrogen partitioning into fluids. Concentration-dependent partitioning of nitrogen will also serve to moderate any initial variations of N/K in slab materials upon dehydration, and this may help to explain the relatively uniform N/K ratio of MORB mantle. We supplement our nitrogen concentration experiments with a temperature series (1.5-2 GPa, 750-950 °C). Our temperature series data reveal that at high temperature nitrogen favors melts over fluids, while temperature has no resolvable effect of biotite-fluid partitioning.

#### 1. Introduction

Nitrogen (N) is the dominant atmospheric component on Earth and is essential for life. Evidence suggests that N has remained abundant in the atmosphere for billions of years (Marty et al., 2013). A N-rich atmosphere persists despite the accumulation of N-rich organic matter in oceanic sediments and the subduction of these sediments into the mantle over billions of years (Halama et al., 2014; Stücken et al., 2016). Combining current plate rates and estimates for N contents of subducted materials implies the whole mass of N in the atmosphere today should

cycle into subduction zones on the billion-year timescale (Goldblatt et al., 2009).

Maintaining a N-rich atmosphere on a planet with plate tectonics and an active biosphere over billions of years apparently requires that much of the N initially subducted is ultimately released back to the atmosphere. This is likely facilitated by the mass-loss processes of dehydration and melting that slabs experience during their descent below forearcs, arcs, and backarcs. Indeed, experimental work highlights that N prefers fluid to silicate phases (minerals and silicate melts) over a wide variety of geologically applicable pressure, temperature, and oxygen

<sup>\*</sup> Corresponding author at: Tulane University, 101 Blessey Hall, New Orleans, LA 70118, United States. *E-mail address*: cjackson2@tulane.edu (C.R.M. Jackson).

fugacity ( $fO_2$ ) conditions, such that fluid-loss from slabs is key to maintaining a N-rich atmosphere (Mysen et al., 2008; Li et al., 2013, 2015; Mallik et al., 2018; Förster et al., 2019; Jackson et al., 2021).

The partitioning of N between silicate and fluids can be interpreted in the context of N speciation (Mikhail and Sverjensky, 2014). Nonpolar, neutrally speciated nitrogen (e.g.,  $N_2$ ) is expected to be relatively unreactive with silicate phases, taking the analogy of noble gases (Carroll and Stolper, 1993; Heber et al., 2007; Jackson et al., 2013, 2015). In contrast to neutral species, the ammonium ion (NH $_4^+$ ) can readily substitute for K $_1^+$  in silicate structures (Pöter et al., 2004). The relative stability of  $N_2$  and  $NH_4^+$  species can be described by the following chemical reaction:

$$2N_2 + 6H_2O + 4H^+ = 4NH_4^+ + 3O_2 (1)$$

Higher pH (lower activity of H<sup>+</sup>), and perhaps higher temperature conditions, offer the possibility of stabilizing additional NH species, including NH<sub>3</sub>, NH<sub>2</sub><sup>-</sup> and NH<sup>2-</sup> species (Mysen and Fogel, 2010; Dalou et al., 2019; Mosenfelder et al., 2019; Grewal et al., 2020):

$$NH_{4}^{+} = NH_{3} + H^{+} \tag{2}$$

$$NH_3 = NH_2^- + H^+ (3)$$

$$NH_2^- = NH^{-2} + H^+ (4)$$

All NH species will have their own tendency to partition between silicate and fluid phases. It is also possible to stabilize melt-soluble nitride species ( $N^{-3}$ ) in the absence of H (Libourel et al., 2003):

$$2N_2 + 6O_{melt}^{-2} = 3O_2 + 4N_{melt}^{-3} \tag{5}$$

Reaction (1)–(5) stoichiometry suggests that systems with high concentrations of N will favor  $N_2$  stability, while systems with low concentrations of N will favor reduced, single N atom species, for any given PT or  $fO_2$  condition (Li and Keppler, 2014). This can be demonstrated by expressing the mass action statement for Reaction (1) and rearranging to solve for the  $NH_4^+/N_2$  concentration ratio:

$$\frac{\gamma_{N_2}}{XNH_4^+ \bullet \gamma_{NH_4^+}^2} \left(\frac{K_1 \bullet f H_2 O^6 \bullet a H^{+4}}{f O_2^3}\right)^{0.5} = \frac{XNH_4^+}{XN_2}$$
(6)

where  $\gamma$  denotes activity coefficient, X denotes mole fraction,  $K_1$  is the equilibrium constant for Reaction (1), f denotes fugacity, and a denotes chemical activity.

The impact of N concentration on partitioning that is highlighted here is distinct from a violation of Henry's Law, as the changing solution properties for N in host phases are not the driving forces for concentration dependence. The mechanism for concentration-dependent reactivity of nitrogen is analogous to that associated with H<sub>2</sub>O molecules dissolving into magma as two hydroxyl groups (Stolper, 1982).

The potential for N concentration to affect partitioning is important because experiments that investigate N partitioning between minerals, melts, and fluids are typically doped with N concentrations higher than observed in nature. If a concentration effect is present, previous work would bias toward heightened stability of  $N_2$  at high concentration (Mysen et al., 2008; Mysen and Fogel, 2010; Schmidt and Watenphul, 2010; Li et al., 2013; Li and Keppler, 2014; Li et al., 2015; Mallik et al., 2018; Förster et al., 2019; Jackson et al., 2021).

The potential for N concentration to affect speciation is also important because N is present in a wide range of concentrations in natural systems. For example, the metasedimentary rocks of the Catalina Schist and westerns Alps have N concentrations that range from 1721 to 30 ppm (Bebout and Fogel, 1992; Busigny et al., 2003). Exhumed eclogites and serpentinites have N concentrations that range down to single ppm (e.g., Busigny et al., 2011; Halama et al., 2014, 2017). Bulk sediments input into the Central American subduction range from 62 ppm N in carbonate-rich materials to 2382 ppm N in organic carbon-rich

diatomaceous ooze (Li and Bebout, 2005). Moreover, magmatic gases also have a wide range in concentrations, with gases from just the Central American Volcanic Arc ranging from 2 to 2500 ppm (Fischer et al., 2002). High temperature fumarole gases with minimal atmospheric contamination can have nearly 2 vol% N<sub>2</sub> (Labidi et al., 2021).

To test the hypothesis that the concentration of N affects its speciation, and therefore its reactivity and retention in silicate phases, we have conducted a series of partitioning experiments with variable concentrations of N ([N] Series). Our results reveal that partitioning of N between melt-fluid ( $D^N_{melt/fl}$ ) and biotite-fluid ( $D^N_{biotite/fl}$ ) pairs varies with the N concentration in the fluids. We further complete a new series of experiments that constrain the role of temperature in modulating partitioning of N between fluid, melt, and biotite. Our data reveal, in combination with our previous work (Jackson et al., 2021), that higher temperatures promote N partitioning into melt while biotite-fluid partitioning remains relatively insensitive to temperature.

#### 2. Methods

### 2.1. Experimental methods

We conducted experiments using a piston cylinder (Tulane University) to react N-bearing fluid, melt, and minerals under controlled P, T, and  $fO_2$  conditions. Temperatures ranged from 750 to 950 °C, and pressures ranged from 1.5 to 1.9 GPa. Experimental durations ranged between 66 and 98 h. These experimental durations are in excess of what our previous work identified as required to achieve a steady state distribution of nitrogen between melt and fluid (Jackson et al., 2021). All experiments were buffered using a nickel-nickel oxide oxygen buffer (NNO) using a double capsules design. Nitrogen was added to experiments using ammonium nitrate (NH<sub>4</sub>NO<sub>3</sub>).

Experimental methods follow from Jackson et al. (2021) and are recounted here. We load inner Pt capsules with a starting composition (HY3, Supplementary Table 1) containing hydroxide components (~20 mg), along with a known mass of NH<sub>4</sub>NO<sub>3</sub> as the source of N. Variable amounts of NH<sub>4</sub>NO<sub>3</sub> were added to separate capsules to generate a series of experiments with variable nitrogen concentrations (referred to as [N] Series). Hydroxides used include SiO<sub>2</sub>-xH<sub>2</sub>O (silicic acid hydrate powder), Mg(OH)<sub>2</sub>, Al(OH)<sub>3</sub>, KOH, Na<sub>2</sub>SiO<sub>3</sub>-xH<sub>2</sub>O. Iron was added as Fe<sub>2</sub>O<sub>3</sub>, and Ca was added as decarbonated CaCO3. We measured the LOI of silicic acid hydrate to be 59%, and given the large amount of SiO<sub>2</sub> in our starting composition, silicic acid hydrate is the dominant contributor to the water content of our experiments. Upon heating, the starting composition breaks down to produce oxides, water, and N. We assume that NH<sub>4</sub>NO<sub>3</sub> decomposes to three moles of H<sub>2</sub>O (with a mole of H<sub>2</sub> fluxing from the outer capsule to completely react the three moles of O) and one mole of N<sub>2</sub>. Starting powders were stored in jar under laboratory air. Our starting powders are hydroscopic, and CaO and KOH are especially hydroscopic. This opens the possibility that our starting composition could have variable amounts of H2O as it reacts with laboratory air. To test for this effect, we conducted LOI measurements at the outset of experiments, within the study, and at the conclusion of the experiments, yielding LOIs of 48, 50, and 52%, respectively. We assume the average LOI 50% for our experiments and propagate 4% fractional uncertainty on the nitrogen concentration of our experiments due to the uncertainty of the water content of the starting powder. Our measured LOI values are similar to the 44% calculated for our starting composition from stoichiometry and measured LOIs of individual components.

Our charges contain  $Fe_2O_3$  that should partially reduce to form FeO given the buffering of our experiments to near NNO. The likely reductant is  $H_2$ , drawn in the from the outer capsule. This  $H_2$  should react to form  $H_2O$ , and therefore can contribute additional water to our experimental system. This effect is however relatively small. Complete reduction of the  $Fe_2O_3$  of our starting composition (16.52 wt% of dry silicate) to FeO will produce 0.009 mg of water per mg of starting composition (silicate

plus water). This mass of water is 1.9% of the mass of water added directly as hydroxides, and this analysis is an upper limit given that not all  $\rm Fe_2O_3$  is reduced to FeO under near NNO. We therefore do not include this contribution of water in our calculations.

By measuring the loss on ignition of the hydroxide starting composition, we introduce precisely known amounts of water into the experimental system. Introducing water using a micro-syringe requires measurements of sample mass before, after syringing, and upon welding. These measurements make water contents associated with microsyringing potentially more uncertain compared to water contents associated with hydroxide starting compositions, provided the hydroxides contain a repeatable mass fraction of water. A small amount of Fe metal ( $\sim 1$  mg) was also loaded into the inner capsule to counter the effect of Fe loss to Pt before sealing. The inner capsule was then sealed into a Au outer capsule along with the NNO oxygen buffer ( $\sim 50$  mg) and H<sub>2</sub>O ( $\sim 15$  mg).

We then loaded the double capsules into an  ${\rm Al_2O_3}$  annulus and packed MgO powder into the free space. The annulus was positioned into a straight-walled graphite heater to locate the top of the capsule in the hotpot using crushable MgO spacers. We used NaCl as the pressure medium. The full assembly was wrapped in Pb foil and loaded into a 0.5 in. pressure vessel.

We pressurized experiments to near the run pressure and then ramped to the run temperature at 100 °C per minute. Final pressure was achieved at the run temperature (hot piston in). We assume a 5% fraction correction given the weak nature of the NaCl pressure medium. Temperature was monitored using a D-type thermocouple. A temperature series (T Series) of experiments were conducted by varying temperature at fixed pressure and nitrogen concentration. Experiments were quenched by cutting the power while maintaining pressure. Upon recovery, we confirmed fluid saturation was maintained in both the outer and inner capsule of each experiment by visually observing the sample "fizz" when the capsule was breached. Further, the melt phase always contains bubbles, affirming vapor saturation.

### 2.2. Analytical methods

We quantify fluid chemistry by mass balance. We did not attempt to quantify fluid chemistry from weight loss observations following piercing of the quenched capsules (e.g., Botcharnikov et al., 2006). These techniques produce large uncertainties when quantifying the concentration of fluid components with mg-level mass and suffer from additional uncertainties due to the retention of fluids in bubbles in the run products that are not lost upon piercing. Nitrogen mass in our experiments varies between 0.68 (PC\_N\_EXP24) to 2.66 (PC\_N\_EXP39) mg.

Our experiments are designed to have a high fluid to silicate ratio (~50 wt% H<sub>2</sub>O in starting composition), and relatively little nitrogen is incorporated into silicate phases (~1000 ppm) compared to the initial nitrogen contents of the unreacted fluid (~10 wt% or 100,000 ppm). Thus, the large majority of nitrogen introduced into our experiments remains as part of the fluid, and we assume the fluid retains its initial unreacted nitrogen concentration for calculation of partition coefficients. We calculate the unreacted fluid composition by first weighing the mass of starting powder added to the inner capsule and then applying the LOI of our starting composition to determine the associated mass of water in the experiment. We then measure the mass of ammonium nitrate (NH<sub>4</sub>NO<sub>3</sub>) added to the inner capsule. We assume that ammonium nitrate decomposes to N2 and H2O, and then add the mass of these products to the overall mass of the fluid components. We propagate the uncertainties associated with masses of materials added to the inner capsule by making replicate measurements of a standard mass on our scale. Replicate measurements of our standard mass yielded an average weight of 0.00157 g with a standard deviation of 0.00006 g (1 $\sigma$ , n = 15) taken over a timeframe similar to the time required to load a capsule (~30 min). There is uncertainty associated with the mass of the capsule before and after adding the NH<sub>4</sub>NO<sub>3</sub>, and we there propagate 0.00006~g of uncertainty twice as independent quantities for a total uncertainty of 0.00008~g for the mass of  $NH_4NO_3$  added to each of our experiments. Uncertainties in the N wt % of fluid are reported in Table 1. We do not account for the additional uncertainties that relate to water in the fluid dissolving into the silicate melt (lowering the fluid mass) and silicate dissolving into the fluid (increasing its mass). These two processes will affect the concentration of N in the fluid, but their effects work in opposite directions and partially cancel. Direct measurement of the N contents of experimental fluids was not attempted due to the difficulty associated with the recovery of volatile  $N_2$ .

Microprobe analytical conditions were 10 kV. Beam currents varied between 1 and 25 nA, and beam diameter varied between 1 and 15  $\mu m$ . Beam conditions varied depending on the material analyzed and the dimensions of material available for analysis. A 10 kV beam was selected to minimize the matrix correction required to quantify N abundances due to the shallower interaction volume and the corresponding shorter path length for x-rays to be emitted from samples. The count rates of Na. K, and N were monitored during their analysis and corrected to their time-zero intensity using the Probe for Windows software. Nitrogen did not appear mobile under the beam conditions utilized here, whereas K and Na count rates decreased with time. Exponential backgrounds were developed for N analysis using long-duration wavescans. Linear backgrounds were assumed for the remaining elements. Nitrogen count times were 90 s on-peak and 60 s off-peak. Other element count times were 20 s on-peak and 10 s off-peak. Nitrogen was peak centered using Si<sub>3</sub>N<sub>4</sub>. We find no obvious shift between the peak centers we determined for Si<sub>3</sub>N<sub>4</sub> and tobelite (NH<sub>4</sub>-bearing mica) we synthesized (Supplementary Fig. 1). Tobelite is a better matrix match for our materials, but given the similarity in peak position, the higher count rate, and beam stability of Si<sub>3</sub>N<sub>4</sub>, we use Si<sub>3</sub>N<sub>4</sub> to center. Standards and diffracting crystals are as follows: manganite (Mn, LIFL), chromite (Cr, LIFL), fayalite (Fe, LIFL). FeNi (Ni, LIFL), sodalite (Cl, PETL), diopside (Ca, PETL), albite (Na, PETL), enstatite (Mg, TAPL), microcline (K and Si, TAPL). Our approach to nitrogen analysis follows that detailed in Jackson et al. (2021).

We calculate the N sensitivity of the LDE5L crystal by correlating its

Table 1
Run conditions.

experiment	series	T, °C	P, GPa	dur, hr	ΔΝΝΟ	N fl., wt %	N fl. ±, wt. %
PC-NK- EXP24	[N]	800	1.67	70	-0.05	8.0	0.4
PC-NK- EXP25	[N]	800	1.75	71	-0.06	8.8	0.4
PC-NK- EXP27	[N]	800	1.73	66	-0.14	16.1	0.7
PC-NK- EXP29	[N]	800	1.74	75	-0.06	9.0	0.4
PC-NK- EXP30	[N]	800	1.76	98	-0.06	8.2	0.4
PC-NK- EXP32	[N]	800	1.79	72	-0.12	14.0	0.6
PC-NK- EXP33	[N]	800	1.75	72	-0.11	13.9	0.6
PC-NK- EXP34	[N]	800	1.77	75	-0.14	15.6	0.6
PC-NK- EXP35	T	775	1.53	70	-0.08	10.6	0.5
PC-NK- EXP36	T	765	1.52	70	-0.09	11.6	0.5
PC-NK- EXP37	T	900	1.57	71	-0.11	13.7	0.6
PC-NK- EXP38	T	950	1.57	70	-0.12	14.5	0.6
PC-NK- EXP39	T	875	1.53	70	-0.16	17.1	0.7
PC-NK- EXP40	T	750	1.51	90	-0.10	13.0	0.6
PC-NK- EXP41	T	925	1.92	72	-0.13	15.4	0.6

count rate with simultaneous LDE1L analyses of N over a range of silicate glasses with high N concentrations. This correlation yields a working curve for N analysis by LDE5L on materials with broadly similar matrices to the unknowns. The sensitivity of the LDE5L crystal using the approach is N wt.% = 0.105  $\pm$  0.039 cps/nA (1 $\sigma$ ). The accuracy of LDE1L measurements of calibration glasses is verified by the measurement of hyalophane secondary standard (900  $\pm$  300 ppm measured versus 1200 ppm nominal, Beran et al., 1992). Additional details on electron microprobe analysis are provided in Jackson et al. (2021).

Raman spectra were collected on the experiments with the highest (PC\_NK\_EXP27) and lowest (PC\_NK\_EXP26) N concentration fluids within the [N] Series. Spectra were collected using a Witec Alpha 300R Raman microscope mated to a 532 nm laser at 25 mW. Light was collected through a  $50\times$  objective lens and passed through a secondary confocal aperture. A grating with 600 grooves per mm was used to diffract the light. Spectra were recorded from Raman shifts of 370–4000 cm $^{-1}$  with a total integration time of 400 s.

# 2.2.1. Oxygen fugacity of experiments

All experiments were run using a double capsule approach to control oxygen fugacity. Equal weights of Ni metal and NiO powders were loaded into the outer capsule ( $\sim$ 50 mg) along with H<sub>2</sub>O ( $\sim$ 15 mg). Because the fluid of the inner capsule is not pure H<sub>2</sub>O, the fO<sub>2</sub> of the inner capsule deviates from the NNO buffer. We take the molar fraction of water implicit in our fluid chemistry determinations, assuming all nitrogen is present as N<sub>2</sub> and ideal solution between N<sub>2</sub> and H<sub>2</sub>O to calculate oxygen fugacity. Calculated deviations are less than a quarter log unit given that H<sub>2</sub>O remains the majority component of our experimental fluids (Table 1).

#### 3. Results

We report the run conditions of our [N] Series (constant *PT*, variable N concentration) and T Series (constant P and N concentration, variable temperature) in Table 1. The combined run conditions of the present experiments and those of Jackson et al. (2021) are reported in Supplementary Table 2. Measured compositions of melt, biotite, and pyroxene are reported in Supplementary Tables 3, 4, and 5.

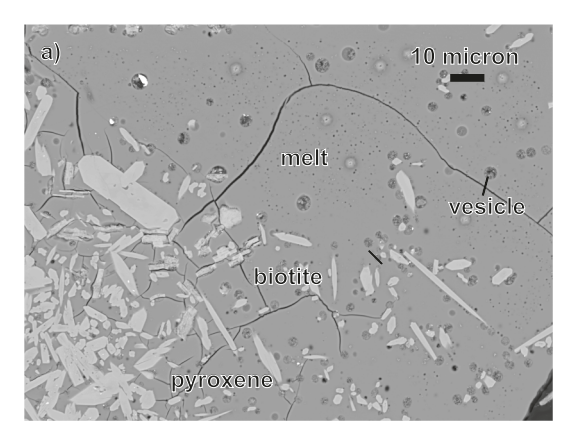
The nitrogen contents of pyroxene are near the detection limit (Supplementary Table 5), indicating that pyroxene is a minor host for N. Pyroxene chemistry is Na-rich, with significant substitution of Na for Ca, balanced primarily by ferric iron. Zoning of Mg-Fe is present in pyroxene and this leads to relatively high standard deviations associated with MgO and FeO analyses (Supplementary Table 5).

# 3.1. Description of experiments

Experiments segregated into a region of silicate phases (Fig. 1) and a large cavity (not shown). We interpret the cavity to be a large vesicle that concentrated the fluid within the experiment. Within the silicate-rich region,  $\sim\!10~\mu m$ -scale vesicles were relatively common and are often adhering to the surfaces of minerals. A smaller population of vesicles ( $<\!\sim\!1~\mu m$ ) are also common throughout the quenched melt and are concentrated in the regions furthest from the edge and other crystals. We interpret these smaller vesicles to form upon temperature quenching of the hydrous melt phase. Pyroxene grows relatively large, often faceted crystals, while biotite forms smaller, typically lath-shaped crystals. Populations of biotite crystals grow both within the melt phase but also in the cavity region immediately surround the melt. The biotite that grow along the melt-fluid boundary and in the fluid tend to be larger (Fig. 1b) and were the focus of our analysis.

#### 3.2. Raman Spectra

Fig. 2 plots the Raman spectra of quenched melts from experiments with fluids containing the highest (PC\_NK\_EXP27) and lowest



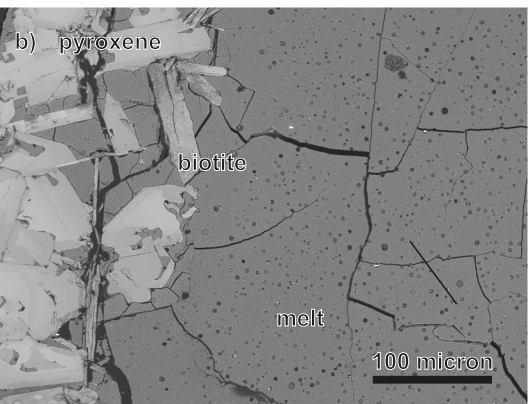


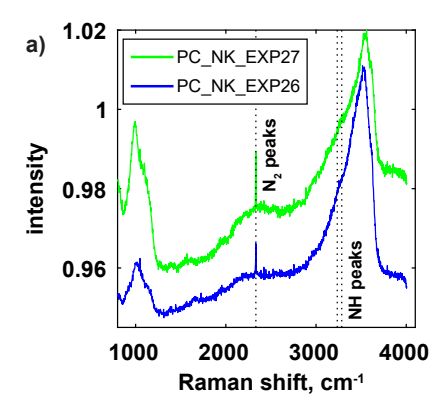
**Fig. 1.** Representative backscattered images. **a)** A small-scale image of experiment PC\_NK\_EXP40 (750 °C, 1.5 GPa). The quenched melt is the darker gray phase that envelops the lighter gray mineral phases. Small scale ( $\sim$ 10  $\mu$ m) vesicles are present throughout the melt. Sub-micron vesicles are also present in the melt away from the minerals. Biotite, pyroxene, and fluid (larger vesicles) are all present. **b)** A large-scale image of experiment PC\_NK\_EXP39 (875 °C, 1.5 GPa). Larger biotite crystals tend to grow at the boundary between the melt and surrounding fluid (right edge of image). Larger biotite crystals were the focus of analysis. Fluid regions are identified as being infilled with epoxy and being backscatter dark. Zoning of Mg-Fe in present in the pyroxene crystals.

concentration of N (PC\_NK\_EXP26) within the [N] Series. Plotted spectra have been normalized to their intensity at 3550 cm<sup>-1</sup> and offset for clarity. We observe a large, asymmetric peak centered near a shift of 3550 cm<sup>-1</sup> that is classically interpreted to reflect OH bonds in silicate glass. We also plot dotted vertical lines for the most intense peak centers reported by Dalou et al. (2019) for NH bonds in silicate glass at 3235 and 3285 cm<sup>-1</sup>. We observe subtle features near these expected NH peak centers that manifest as breaks in slope within the OH peak. The 3235 and 3285 cm<sup>-1</sup> peaks have been assigned to NH<sub>2</sub> and NH<sup>-2</sup>, respectively (Mosenfelder et al., 2019; Dalou et al., 2019), and although peaks in the 3200-3300 cm<sup>-1</sup> have also been assigned to NH<sub>3</sub> (Mysen and Fogel, 2010). Regardless of the specific species, Fig. 2 suggest NH species are present the melts of the [N] Series. We additionally observe sharp peaks near shifts 2323 cm<sup>-1</sup>. These peaks are assigned to N<sub>2</sub> and provide clear evidence that indicate N2 was dissolved in the melt of our experiments. Raman spectra are reported in Supplementary Table 6.

# 3.3. Nitrogen Concentration ([N]) Series

#### 3.3.1. Melt-fluid partitioning of nitrogen

Fig. 3a plots the concentration of N in fluid against the concentration of N in melt for the [N] Series experiments (Table 1). All [N] Series experiments were buffered using Ni-NiO (NNO) pairs. Experimental conditions were 800 °C and 1.7–1.8 GPa. A positive correlation that passes through the origin is expected if  $D_{melt/fl}^N$  values are independent of



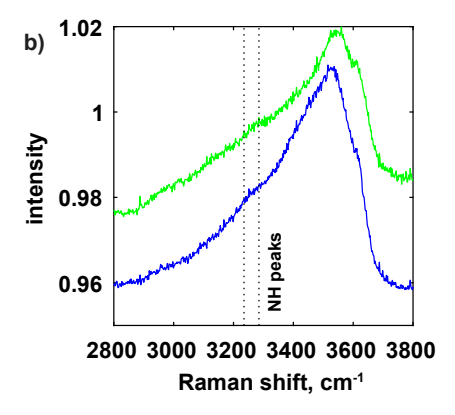


**Fig. 2.** Raman spectra of quenched melt from experiments with highest (PC\_NK\_EXP27) and lowest (PC\_NK\_EXP26) fluid concentration of N. Spectra are normalized to the their intensity at 3550 cm<sup>-1</sup> and offset for clarity. The vertical dotted lines for NH peaks at taken from Dalou et al. (2019). **a)** A larger spectral range view and **b)** A zoom in on spectral region associated with OH and NH bonds

concentration. The data are positively correlated, but the correlation does not pass through the origin (dashed line in Fig. 3a, intercept of 0.10  $\,$ 

 $\pm$  0.02, 1 $\sigma$ ).

In light of the regression not passing through the origin of Fig. 3a, we seek to develop an alternative model. If a decrease in N concentration leads to the conversion of  $N_2$  to melt-soluble, single atom nitride species, following Reactions (1)–(5), we would expect  $N_{wt\%}^{melt}$  to linearly correlate

with  $N_{wt\%}^{fluid}$  raised to an exponent near 0.5. This analysis assumes that  $N_2$  partitions only into the fluid, while nitride species partition only into the melt. In reality, each nitride species will have its own tendency to partition between melt and fluid, with charged species likely favoring the melt to the fluid to a degree, but not in absolute (Mysen and Fogel, 2010; Mosenfelder et al., 2019; Dalou et al., 2019; Grewal et al., 2020). Some  $N_2$  likely also partitions into the melt, rather than be perfectly retained in the fluid (Roskosz et al., 2006; Mysen et al., 2008; Mallik et al., 2018; Fig. 2). This all combines to make it difficult to predict the exponent that relates N concentration in melt and fluid. In the face of this uncertainty, we complete a grid search to identify the possible range of exponent values for our N Series experiments.

The forward model has the following form:

$$N_{wt\%}^{melt} = \beta \left(N_{wt\%}^{fluid}\right)^{\alpha} \tag{1}$$

Our grid search identifies combinations of  $\alpha$  and  $\beta$  that minimize the model chi-squared value. Fig. 3b plots the uncertainty envelopes for  $\alpha$  and  $\beta$  in fitting Eq. (1) (solid 95% and dashed 68% confidence). A wide range of  $\alpha$  values (exponent) result in an acceptable fit due to the trade off with  $\beta$  (slope), but all acceptable  $\alpha$  values are less than one. Our experiments therefore demonstrate that  $D^N_{melt-fl}$  values depend on N concentration.

The best-fitting  $\alpha$  value is 0.50 for melt-fluid partitioning, and at face value this suggests that the PTX conditions of our experiments ( $\sim$ 1.75 GPa and 800 °C with a rhyolitic melt) permit the stabilization of meltreactive NH species, as suggested by Fig. 2. We stress, however, that the uncertainty on  $\alpha$  remains large (Fig. 3b), allowing  $\alpha$  to approach 0.68 at the 68% confidence threshold, which could indicate stabilization of some NH species that partition into the fluid. Indeed, prior experiments provide evidence that a portion NH species are not silicate reactive under geological conditions. Prior experimental work by Li et al. (2015) and Jackson et al. (2021) conducted at lower pressure (0.2-1 vs 1.75 GPa in this study) showed that  $log(D^N_{melt/fl})$ ) and  $log(D^N_{biotite/fl})$  correlate with  $fO_2$  along moderate slopes (~-0.15), in contrast with the slope of -0.75 expected from the charge difference between N speciation in nitride complexes (-3) and N<sub>2</sub> (0). The more moderate slope of the fO<sub>2</sub> dependence on partitioning suggests that a portion of reduced N species remain with the fluid, which would be consistent with  $\alpha$  values greater than 0.5 and the production of less silicate reactive nitride species. Fig. 3c plots the fit assuming an exponent of 0.5.

#### 3.3.2. Biotite-fluid partitioning of nitrogen

Biotite readily incorporates N as NH<sub>4</sub>, but rejects N<sub>2</sub>, (Bos et al.,

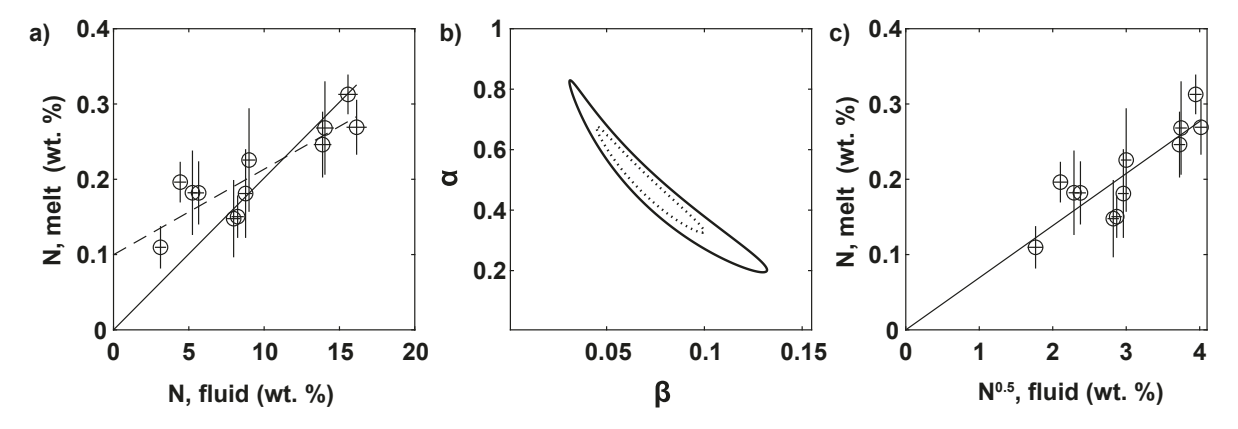


Fig. 3. Concentration dependence of melt-fluid partitioning of N. a) Correlation of N concentration in melt against N concentration in fluid. The dotted line is the least-squares fit, and the solid line is the least-squares fit forced through the origin. b) Uncertainty envelopes for the non-linear fit of melt and fluid concentration of N. Alpha ( $\alpha$ ) and beta ( $\beta$ ) are parameters in Eq. (1). The dotted envelope is the 68% confidence interval, and the solid envelope is the 95% confidence interval. Alpha values are constrained to be less than one (>95% confidence), indicating that N concentration affects its partitioning between melt and fluid. c) Correlation of N concentration in melt against the square root of N concentration in fluid. The solid line is the least-squares fit forced through the origin. All data are recalculated to NNO and 1.75 GPa to account for small variations in  $fO_2$  and pressure between experiments.

1988; Mingram and Bräuer, 2001; Pöter et al., 2004; Plessen et al., 2010), and from this it is expected that the correlation between  $N_{wt\%}^{biotite}$  and  $N_{wt\%}^{fluid}$  will also not pass through the origin when N is in a mixed speciation regime (dashed line in Fig. 4a, intercept of  $0.12 \pm 0.06$ ,  $1\sigma$ ), following the behavior established for the melt-fluid partitioning (Fig. 3).

We conduct a grid search on the biotite-fluid data, using the same approach applied to the melt-fluid system (Fig. 4b), to identify permissible  $\alpha$  and  $\beta$  values. The  $N_{WV\%}^{biotite}$  data are relatively scattered, perhaps reflecting the low beam current analysis on biotite (due to their restricted size and care taken to not devolatilze N) and/or a more sluggish approach to equilibrium. The scatter translates into a larger uncertainty ellipse. Nonetheless, the data constrain the  $\alpha$  value to also be less than 0.80 (68% confidence) and a best-fitting  $\alpha$  value of 0.43. Thus, while a precise  $\alpha$  value cannot be recovered for the biotite-fluid data, these data suggest that  $D_{biotite/fl}^N$  values depend on N concentration to a similar degree established for  $D_{melt/fl}^N$  values (Fig. 3). Assuming an  $\alpha$  value of 0.5 yields a model with an improved mean squared error of 0.0058 compared to 0.0093 for the linear model forced through the origin. Following this, we take an  $\alpha$  value of 0.5 for discussion purposes below.

#### 3.3.3. Temperature effect on nitrogen fluid mobility

Figs. 3 and 4 suggest that lower concentrations make nitrogen progressively more reactive with silicate phases under geologically applicable *PTX* conditions. With this understanding, we now seek to quantify how temperature modulates N fluid mobility. Towards this end, we conducted additional experiments that vary temperature and hold other variables nearly constant (T Series, Table 1).

Fig. 5 displays partitioning results against inverse temperature. The fluid concentration is raised to power of 0.5 ( $\alpha$  value of 0.5). Results include the present T Series and the T Series from Jackson et al. (2021). Fig. 5a plots the melt-fluid partitioning results. The negative correlation is significant ( $R^2 = 0.73$ , p-value = 0.002, n = 11) and indicates higher temperatures favor N incorporation in melt over fluid. This result is not predicted by speciation calculations, as lower temperatures are expected to stabilize presumably more silicate-reactive NH<sub>4</sub> relative to N<sub>2</sub> and NH<sub>3</sub> (Mikhail and Sverjensky, 2014). Studies of N<sub>2</sub> solubility in melt also indicate no temperature dependence (Gao et al. 2022), so the rise of N partitioning into melt with temperature is presumably related to NH species. Indeed, spectroscopic observations of higher temperature experiments suggest  $\mathrm{NH}_2^-$  and  $\mathrm{NH}^{2-}$  are present in reduced melts (Mysen et al., 2008; Dalou et al., 2019; Mosenfelder et al. 2019; Grewal et al., 2020), and their stability may help explain the higher  $D_{melt/fl}^{N}$  values we observe at higher temperatures. Alternatively, higher temperatures are

associated with greater amounts of dissolved silicate in the fluid, and this may lower the affinity of NH species for the fluid phase.

Fig. 5b displays the biotite-fluid partitioning results for the temperature effect. We also take a 0.5 exponent for the fluid concentration following the approach to melt-fluid partitioning. The correlation remains insignificant despite the addition of new data. Our ability to quantify a temperature effect is hindered scatter in the biotite-fluid dataset and specifically by a single datapoint that plots at the low end of the variability. Nevertheless, the lack of correlation is consistent with a relatively minor effect of temperature on  $D^N_{biotite/fl}$  values. If a more silicate-rich fluid lowers the affinity of N for the fluid, then the lack of a temperature effect on  $D^N_{biotite/fl}$  value may be explained by a corresponding destabilization NH $_4^+$  or production of N species that do not dissolve into biotite.

In Fig. 5c we regress  $log(D_{biotite/melt}^N)$  against 1/T for the T Series experiments from this study and Jackson et al. (2021). The data are correlated ( $R^2=0.45$ , p-value = 0.03, n = 11), with a slope that is opposite that that documented in Fig. 5a. This suggests that the decrease in  $D_{biotite/melt}^N$  value at high temperature is largely driven by an increase in melt solubility.

All partitioning values in Fig. 5a and b have been recalculated to a common P/T and  $fO_2$  (P/T = 1.75 GPa/1073 K and  $fO_2$  = NNO) to account for small variations in these parameters between experiments of the T Series using the applicable P/T and  $fO_2$  parameters from Jackson et al. (2021) (Table 1, Supplementary Table 2). Partitioning values in Fig. 5c have similarly been recalculated to a common P/T (1.75 GPa/1073 K) using the applicable P/T parameter from Jackson et al. (2021) to account for small P variations within the T series (Table 1, Supplementary Table 2).

# 3.4. Parameterization of partitioning data

To predict  $D_{melt/fl}^N$  values across naturally applicable PTX conditions, we combine the PC  $fO_2$  and P (pressure), T Series of Jackson et al. (2021) with the present T Series. The data are reported in Supplementary Tables 2 and 3.

Our general form is as follows for concentration-dependent partitioning:

$$log\left(D_{melt/fl}^{N}\right) = f(P, T, X) + (\alpha - 1) log(N_{wt\%}^{fl.})$$
(2a)

0

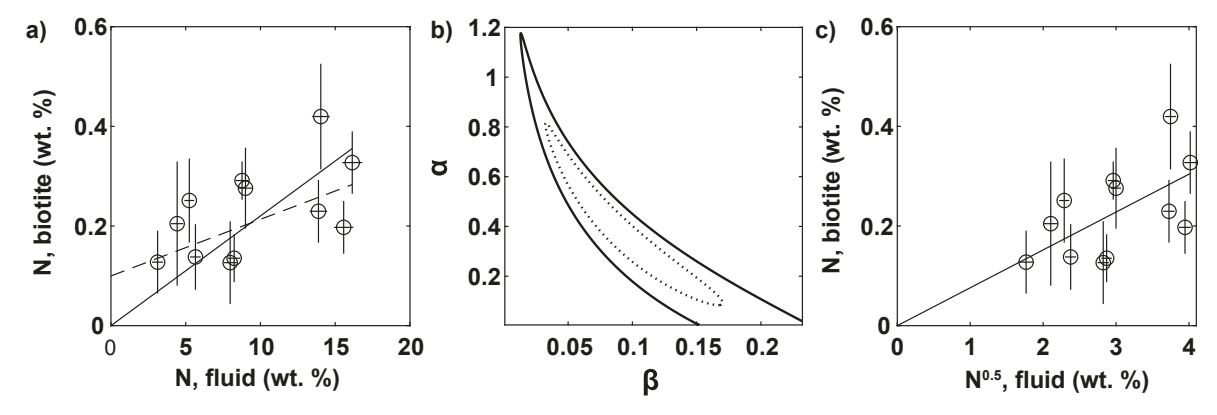
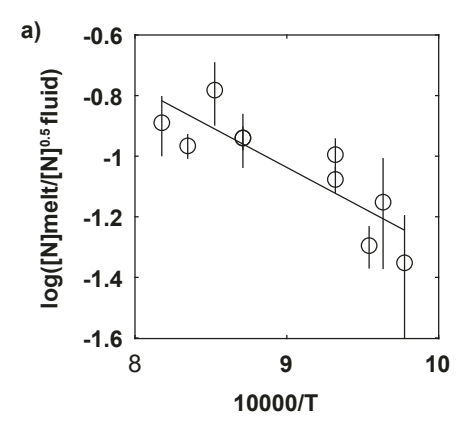
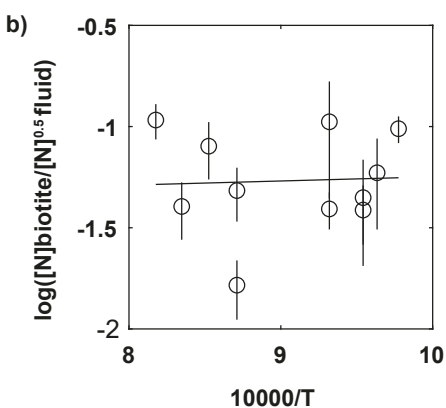
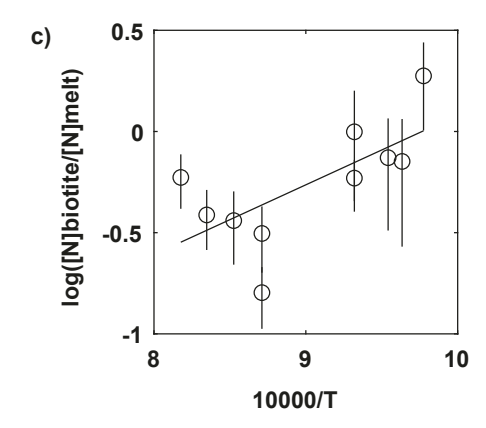


Fig. 4. Concentration dependence of biotite-fluid partitioning of N. a) Correlation of N concentration in biotite against N concentration in fluid. The dotted line is the least-squares fit, and the solid line is the least-squares fit forced through the origin. b) Uncertainty envelopes for the non-linear fit of biotite and fluid concentration of N. The dotted envelope is the 68% confidence interval, and the solid envelope is the 95% confidence interval. Alpha values are constrained to be less than 0.80 (>68% confidence). c) Correlation of N concentration in biotite against the square root of N concentration in fluid. The solid line is the least-squares fit forced through the origin. All data are recalculated to NNO to account for small variations in  $fO_2$  between experiments.







**Fig. 5.** Effects of temperature on N partitioning. **a)** Log of melt-fluid<sup>0.5</sup> partitioning of N against inverse temperature. The data have positive correlation ( $R^2=0.73$ , p-value = 0.002). **b)** Log of biotite-fluid<sup>0.5</sup> partitioning of N against inverse temperature. The data are not significantly correlated ( $R^2=0.03$ , p-value = 0.60). **c)** Log of biotite-melt partitioning of N against inverse temperature. The data are positively correlated ( $R^2=0.45$ , p-value = 0.03).

$$log\left(D_{melt/fl}^{N}\right) = \frac{f(P, T, X)}{\alpha} + (1 - 1/\alpha) log(N_{wt\%}^{melt})$$
 (2b)

where  $\alpha$  is the exponent from Eq. (1). Eqs. (2a) and (2b) permit the partitioning of N to be predicted in cases where N concentration in either the fluid or the melt can be estimated.

We take a value of 0.5 for the  $\alpha$  value in our regression because of the non-linear relationship observed between  $N_{wt\%}^{melt}$  and  $N_{wt\%}^{fl}$  and because it near is the best fitting  $\alpha$  value for melt-fluid partitioning (Fig. 3), but the effect of other  $\alpha$  values is considered below. The parameterization is as follows (R<sup>2</sup> = 0.94, p-value < 0.001, n = 17):

$$log(D_{melt/fl}^{N}) = -2446/T \pm 664 + 655 \pm 70 P/T - 0.23$$
  
$$\pm 0.02\Delta NNO - 0.5 \bullet log(N_{set}^{fl.}) + 0.10 \pm 0.63$$
 (3a)

or

$$log(D_{melt/fl}^{N}) = 2(-2446/T \pm 664 + 655 \pm 70 P/T - 0.23 \pm 0.02\Delta NNO + 0.10 \pm 0.63) - log(N_{wt @}^{melt})$$
(3b)

Similarly, to predict  $D_{boite/fl}^N$  values across naturally applicable *PTX* conditions we conduct a multiple linear regression on the P and  $fO_2$  Series of Jackson et al. (2021) that accounts the non-linear partitioning of N ( $R^2 = 0.82$ , p-value = 0.01, n = 8):

$$log\left(D_{\frac{biorite}{f^{l}}}^{N}\right) = 409 \pm 138 \frac{P}{T} - 0.15 \pm 0.04 \bullet \Delta NNO - 1.71 \pm 0.20 - 0.5$$

$$\bullet log(N_{wt\%}^{fl})$$
(4a)

or

$$\begin{split} log \Big( D_{biotite/fl}^{N} \Big) &= 2(409 \pm 138 P/T - 0.15 \pm 0.04 \bullet \Delta NNO - 1.71 \\ &\pm 0.20 \Big) - log \big( N_{wl}^{biotite} \big) \end{split} \tag{4b}$$

We again take a value of 0.5 for the  $\alpha$  term. The smaller  $fO_2$  coefficient for the biotite-fluid parameterization compared to the melt-fluid parameterization suggests reduced NH species, other than NH $_4^+$ , contribute to overall N solubility in melt.

We do not include experiments associated with the [N] Series or T Series for the biotite-fluid parameterization. Temperature is found to not correlate significantly with  $D^N_{biotite/fl}$  values (Fig. 5b), while the [N] Series data introduce additional scatter towards constraining pressure (P/T term) and  $fO_2$  effects, as these experiments were conducted essentially at a single P/T and  $fO_2$  condition.

Our expanded T Series experiments also permit the parameterization of  $D_{biotite/melt}^N$  values. We combine the P and T Series data of Jackson et al. (2021) and this study to generate the equation ( $R^2 = 0.55$ , p-value = 0.01, R = 0.01):

$$log(D_{biotie-melt}^{N}) = 3558/T \pm 1410 - 318\frac{P}{T} \pm 150 - 2.90 \pm 1.34$$
 (5)

All parameters in all models are significant at the 95% confidence level. Fig. 6 compares observed N partition coefficients to those predicted by Eqs. (3)–(5).

#### 4. Discussion

#### 4.1. Application of parameterizations to mass transfer processes

We now apply of Eqs. (3)–(5) to mass transfer processes that can affect the distribution N in natural settings and explore the importance of concentration-dependent partitioning of nitrogen.

# 4.1.1. Nitrogen loss from magma exsolving fluid

Volatile elements partition into fluids as magmas ascend towards the surface. In this way, the atmosphere is built and modified over geologic time. Our experiments replicate aspects of this process for the water-rich systems associated with arc volcanoes, as the melts in our experiments are fluid-saturated and rhyolitic. There is the potential for hydrous magmas to exsolve a fluid phase over a range of pressures and temperatures as they ascend and cool. We correspondingly apply Eq. (3) to calculate  $D^N_{melt/fl}$  values for temperatures ranging between 600 and 900 °C and pressures ranging between 0.01 GPa to 0.5 GPa. Nitrogen

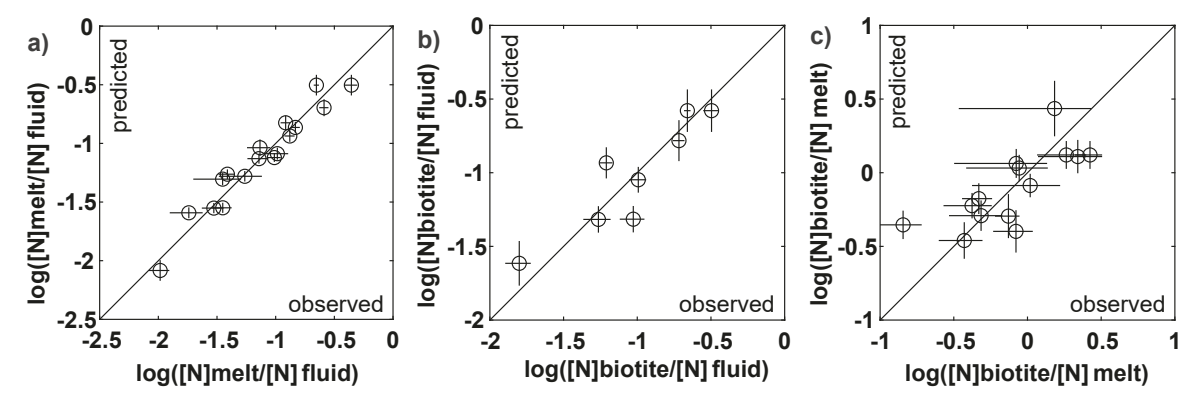


Fig. 6. Comparisons of observed N partition coefficients versus those predicted by Eqs. (3)–(5). Uncertainties are  $1\sigma$ . a) Correlation of observed and predicted meltfluid partition coefficients ( $R^2 = 0.93$ , p-value < 0.001, n = 17). b) Correlation of observed and predicted biotite-fluid partition coefficients ( $R^2 = 0.82$ , p-value = 0.01, n = 8), c) Correlation of observed and predicted biotite-melt partition coefficients ( $R^2 = 0.55$ , p-value = 0.01, n = 14).

concentrates in fluids over melt, and therefore degassing also leads to the depletion of nitrogen in magmas. Given the concentration dependence established for  $D^N_{melt/fl}$  (Fig. 3), it is expected that  $D^N_{melt/fl}$  values will rise throughout the degassing processes. To demonstrate the importance the concentration-dependent partitioning in natural systems we take the range of N concentration in gas samples from the Central American Arc contain (2–2500 ppm, Fischer et al., 2002) as low [N] and high [N] endmember scenarios. Calculation results are reported in Fig. 7 and

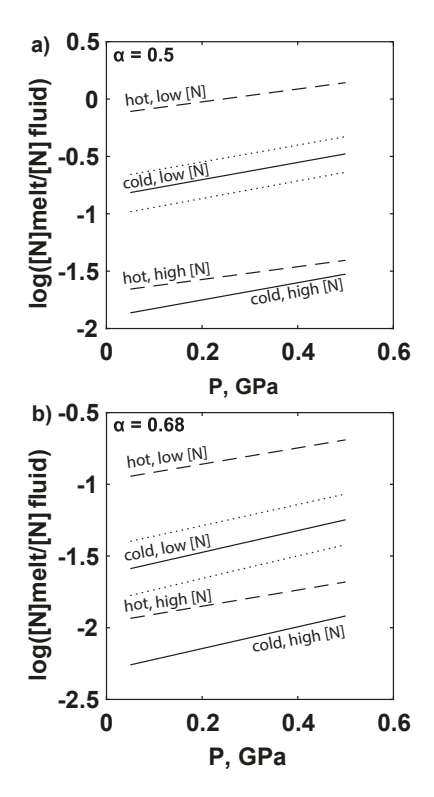


Fig. 7. Application of Eq. (3) to magmatic degassing scenarios as a function of pressure. a) Scenarios assume and  $\alpha$  value of 0.5. Dashed lines are for hot degassing (900 °C) scenarios. Solid lines are for cold degassing (600 °C) scenarios. The upper line for each temperature corresponds to low N concentrations (2 ppm N), and lower line for each temperature corresponds to high N concentrations (2500 ppm N). Nitrogen degassing efficiency is minimized at high temperatures, low N concentration, and high pressure. The dotted lines are a representative uncertainty envelope (68% confidence) propagated from Eq. (3) onto the cold, low [N] scenario. b) Same as a) but scenarios assume an  $\alpha$  value of 0.68. Partitioning in low [N] scenarios is shifted to lower values by approximately a factor of 10 compared to low [N] that assume an  $\alpha$  value of 0.5.

assume an fO2 fixed at NNO.

Under higher PT (0.5. GPa, 900 °C) and low [N] (2 ppm) conditions we predict N partitioning into hydrous fluid to be relatively inefficient (upper dashed line of Fig. 7), with  $D_{melt/fluid}^{N}$  values near 1. Increasing the N concentration from 2 to 2500 ppm lowers  $D_{melt/fluid}^{N}$  values by over an order of magnitude at constant PT conditions. Fluid loss from colder magma is associated with lower  $D_{melt/fluid}^{N}$  values, with cold models (600 °C) shifted by approximately half an order of magnitude compared to hot models (900 °C). Pressure is predicted to have a minor effect over the relatively narrow range of 0.05 and 0.5 GPa.

If an  $\alpha$  value of 0.68 is assumed, the low [N] scenarios are shifted to lower  $D_{melt/fluid}^N$  values by an order-of-magnitude compared to those that assume an  $\alpha$  value of 0.5. High [N] scenarios less affected by the assumed  $\alpha$  value because the high [N] scenarios are closer in concentration compared to the experimental data (Supplementary Table 2).

The increased melt/fluid partitioning of nitrogen with lower N concentrations suggests that N can be lost from magma at variable rates with respect to other volatile elements. This is important because ratios of N to other volatile elements are used to constrain the flux of N through arc magmatic systems and to constrain the volatile-rich components that contribute to arc magmas (e.g., Sano et al. 1998; Fischer et al., 2002; Hilton et al., 2002). This approach often requires the assumption that N is lost at a constant rate relatively to other volatiles Our data indicate this need not be the case under geological conditions because  $D_{melt/fluid}^N$  values can vary substantially over geologic conditions. The sensitivity of  $D_{melt/fluid}^N$  values to temperature, composition, pressure, and concentration, however, may enable gas ratios that include N to be potentially rich recorders of magmatic conditions and evolution.

It is important to note that the non-linear dependency between the concentration of N in melt and fluid in our experiments implies a system with mixed N<sub>2</sub> and reduced NH species control on partitioning. The importance of reduced NH species under oxidizing conditions (~NNO) likely is enabled by the hydrous and cool nature of our experiments. Support for a mixed NH-N<sub>2</sub> system comes from Fig. 2 as well as from regressions of Li and Keppler (2014), who predict a NH<sub>3</sub>/N<sub>2</sub> ratio of 1.1 for the PTX conditions of our [N] Series (800 °C, 1.75 GPa, NNO, ~9 wt % N in fluid). Calculations of N speciation in cooler, H-rich systems also favor NH species stability (Mikhail and Sverjensky, 2014). Cooler (775 °C), hydrous experiments yield evidence for NH species influencing partitioning to fO2 as oxidizing as the Re-ReO2 oxygen buffer (Jackson et al., 2021). In contrast, higher temperature, 1-atm experiments without H indicate that  $N_2$  dominates melt solubility to  $fO_2$  as reducing as IW (Libourel et al., 2003; Boulliung et al., 2020). This all serves to highlight the importance of PTX conditions in controlling N speciation and its reactivity with silicate. Care must be taken to apply Eq. (3) to conditions where mixed N2-NH species control on partitioning is expected. It is likely that the behavior of nitrogen in higher temperature, oxidizing, and H-poor systems will be dominated by  $N_2$  alone, and in this regime its degassing should follow a simple Henrian relationship rather than the concentration-dependent regime explored here.

#### 4.1.2. Nitrogen loss from a dehydrating slab

The partitioning of N between slab minerals and fluids determines how efficiently fluids mobilize N under equilibrium conditions. Our experiments indicate that the partitioning of N between silicate melt and fluid depends on concentration (Fig. 3), and it is likely that partitioning of N between minerals and fluid does as well (Fig. 4).

As emphasized in the previous section, N partitioning should only depend on concentration while  $N_2$  and single atom N species (e.g., NH species) both contribute to partitioning behavior. Under progressively lower N concentrations there will be a threshold where N partitioning is defined solely by single atom N species, and below the threshold concentration,  $D_{mineral/fluid}^N$  will be maximized and likely independent of concentration. Thus, care must be taken when using Eq. (4) in order to avoid application to scenarios where N partitioning is not affected by both  $N_2$  and NH species (i.e., the single atom N species relevant to this study).

To place an upper limit on  $D^N_{biotite/fluid}$  values (corresponding to a regime where partitioning is determined solely by NH species) we consider K partitioning. The partition coefficient of K between biotite and fluid ( $D^K_{biotite/fluid}$ ) is likely to place an upper bound on  $D^N_{biotite/fluid}$  values because when N is stabilized as the ammonium ion (NH $^+_4$ ), as is favored under lower concentration conditions (Reaction (1)), its partitioning into biotite will be similar to K given the equal charge and similar size of  $K^+$  and  $NH^+_4$ .

Experiments under elevated PT conditions indicate K has a preference for biotite over fluid, with  $D^K_{biotite/fluid}$  values ranging up to 30, (Johnson and Plank, 2000; Luginbühl, 2015). We correspondingly take  $D^N_{biotite/fluid}=30$  as the maximum possible value (gray fields in Fig. 8). This value is  $>10\times$  greater than the maximum  $D^N_{biotite/fluid}$  values experimentally measured under slab-applicable PTX conditions, albeit at high N concentrations (Förster et al., 2019).

With an upper limit on  $D_{biotite/fluid}^N$  set, we now apply Eq. (4b) to predict  $D_{biotite/fluid}^N$  values under applicable PTX conditions (Fig. 8). Nitrogen concentrations often exceed 1000 ppm in natural micas, but can range down to ~10 ppm (Sadofsky and Bebout, 2000; Plessen et al., 2010). To account for this natural variability, we consider dehydration scenarios with N concentrations in biotite ranging between 10 and 3000 ppm. We apply the PT conditions from hot (e.g. Cascadia, dashed lines in Fig. 8) and cold (e.g. Honshu, dash-dotted lines in Fig. 8) slab-top geotherms (Syracuse et al., 2010). The pressure range of dash and dash-dotted lines corresponds to conditions where major fluid loss from slabs is predicted to occur (van Keken et al., 2011). Calculations assume an  $fO_2$  of NNO.

The 10 ppm N biotite scenarios yield  $D_{biotite/fluid}^N$  values greater than unity, indicating limited fluid mobility along both warm and cold slab geotherms when N concentrations are low. Predicted  $D_{biotite/fluid}^N$  values for low N concentration (10 ppm) under the cold slab geotherm are uniformly above the upper limit (30, gray field in Fig. 8a). This result emphasizes the caution needed in applying Eq. (4) under low N concentrations and suggests that N partitioning in low N concentrations, hydrous systems will be controlled by NH species, even under relatively oxidizing conditions (NNO).

The 3000 ppm N scenarios more closely approximate the conditions associated with slabs prior to N loss. Under these conditions,  $D_{biotite/fluid}^{N}$  values for warm geotherms remain low, approaching 0.01 at the lowest PT conditions considered. Bulk partition coefficients will be lower considering that K-bearing phases are generally low mode (low temperature altered oceanic crust and GLOSS contain 0.5 and 2 wt%  $K_2O$ ,

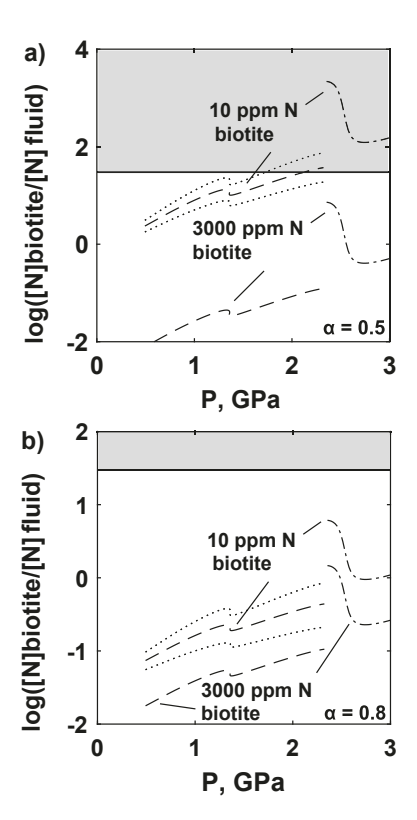


Fig. 8. Application of Eq. (4) to slab dehydration scenarios. a) Calculations assume an  $\alpha$  value of 0.5. Dashed lines are for a warm slab geotherm, and dash-dotted lines are for a cold slab geotherm. The upper dashed and dash-dotted lines assume 10 ppm N in biotite, while the lower lines assume 3000 ppm N. The gray box delineates biotite-fluid partition coefficients that exceed the estimated upper limit (30). The dotted lines are a representative uncertainty envelope (68% confidence) propagated from Eq. (4) onto the 10 ppm, warm slab scenario. b) Calculations follow those in a) but assume an  $\alpha$  value of 0.8. Higher  $\alpha$  values make N partitioning less sensitive to changes in concentration. Shallow extraction of N from a warm slab with high N concentrations is predicted to be most efficient. All calculations assume an  $fO_2$  of NNO.

translating into a mode mica of  $\sim$ 5% and  $\sim$ 20%, respectively) (Jarrard, 2003; Plank and Langmuir, 1998). The fluid mobility predicted for N in a warm environment with higher N concentrations is consistent with the loss of N observed in the Catalina schist along its relatively hot prograde sequence (Bebout and Fogel, 1992).

In contrast to our results for warm slab geothems, our model predicts  $D_{biotite/fluid}^{N}$  values close to unity for cold geotherms in the 3000 ppm N scenarios. This indicates only moderate initial fluid mobility that will be further limited by N loss. This prediction is consistent with the relative lack of fluid mobility observed for N within the cooler prograde sequence of the Schistes Lustrés (Busigny et al., 2003).

We emphasize that the  $\alpha$  value is not well constrained for N partitioning between biotite and fluid, and this leads uncertainty upon application of Eq. (4) beyond those directly explored here (~1000–3000 ppm in biotite, Supplementary Table 4). To explore this uncertainty, we consider an  $\alpha$  value of 0.8 (Fig. 8b) and recalculate the same scenarios considered in Fig. 8a. The 0.8 value is the upper limit associated with the 68% confidence interval on the biotite-fluid data (Fig. 4). The 3000 ppm scenarios are similar to those predicted with the 0.5  $\alpha$  value. This similarity is because our partitioning data are close to the high [N] endmember. The 10 ppm scenarios are, however, shifted to higher  $D_{biotite/fluid}^{N}$  values compared to the 3000 ppm scenarios by nearly an order of magnitude, less than half that associated with the 0.5  $\alpha$  value. Note the change is x-axis scale between Fig. 8a and b.

A major finding is that N loss from slabs is a self-limiting process;

with N loss, it becomes more silicate- reactive and mineral-fluid partition coefficients rise. Although our results are for melt and biotite, other K-bearing silicate phases are expected to also more readily incorporate N under low concentration conditions. One net result of self-limiting N-loss is that initial N concentration variations in slabs should be moderated as slabs pass through subduction zones, despite variations in the prevailing geotherm, fO<sub>2</sub>, and extent of dehydration. Moderated N loss from slabs may help to explain the relatively limited variations of N/K ratios inferred for the MORB source (Marty and Zimmermann, 1999). There is increasing evidence that high time-integrated N/K (i.e., N/<sup>40</sup>Ar) component is present in a subset of MORB samples (Labidi, 2022), and this component may relate to subducted materials that experienced relatively cold and/or reduced conditions during their transit into the MORB mantle source region that may better preserve presubduction N/K ratios.

# 4.1.3. Slab Melting

Slab melting provides an additional mechanism to mobilize slab N beyond dehydration and fluid loss. Like for slab dehydration, the mobilization of N by slab melting is likely strongly influenced by Kbearing phases until they are exhausted by the melting process itself. We do not anticipate that N partitioning between minerals and melts will be sensitive to concentration, in contrast to mineral-fluid partitioning. Nitrogen partitioning into both biotite and melt increases with reducing conditions (Jackson et al., 2021), and this implies that reduced, single N species control N solubility in these phases, even under the relatively oxidizing fO2 of NNO. A narrow temperature range for slab melting, near 650 °C, is dictated by the nearly vertical slope of fluid-saturated solidii of slab lithologies (AOC and felsic sediments) in PT space (Lambert and Wyllie, 1972; Huang and Wyllie, 1973). Slab temperatures are predicted to rapidly rise as they encounter the mantle wedge, and this steep temperature rise may be sufficient to induce melting in the uppermost sections of slabs (Syracuse et al., 2010). The specific depth of melting depends on the dynamics of slab-mantle interactions, but predicted pressures range from ~2 to 4 GPa. One caveat to the scenarios we present is that our experiments only stabilize biotite; whereas phengite is predicted to be the stable mica on the solidus above ~3 GPa (Poli and Schmidt, 2002). We consequently only extend our parameterization to 3 GPa. Recent work suggests N prefers biotite to phengite by a factor of 2 or 3 (Förster et al., 2019), so N is likely more easily mobilized into melt compared to the simple extrapolation of Eq. (5) to higher pressure.

Our  $D_{biotite-melt}^N$  parameterization is applied to the conditions of 650 °C and 2–3 GPa in Fig. 9. We predict  $D_{biotite-melt}^N$  values near unity, decreasing by half a log unit per GPa of pressure change. Near unity partitioning makes small degrees of partial melting relatively inefficient at extracting N compared to fluid loss at lower PT conditions (c.f. Fig. 8), but with increasing degrees of partial melt, and the associated destabilization of mica, the efficiency of slab melt extracting N will accelerate. Nitrogen mobilized during slab melting should be coupled with K, as the retention of both elements in rock during melting appears primarily linked to the stability of mica.

# 4.2. Implications of concentration-dependent partitioning of N between silicate phases and hydrous fluid for the global distribution of N

Central dogma holds that the elements mobilized into melts or fluids within the slab are then efficiently transported back to the crust via arc magmas. Arc magmas then degas their volatile load as they ascend and crystallize. In this way, much of the N that is subducted is returned to the atmosphere, while some is retained in down-going materials, perhaps more associated with the altered lithologies in oceanic crust (Li et al., 2007; Mitchell et al., 2010; Busigny et al., 2011). This retained N is then incorporated into the mantle for longer time-scales.

Concentration-dependent reactivity of N in silicate-fluid systems makes the return of slab N back to the atmosphere a self-limiting process

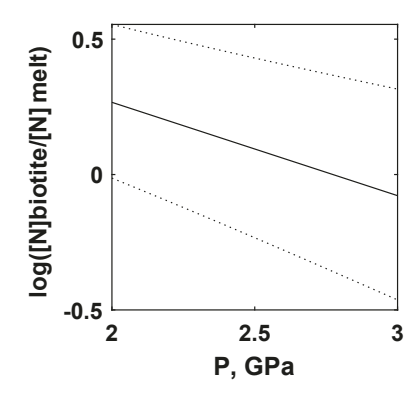


**Fig. 9.** Applications of Eq. (5) to slab melting scenarios. Temperature is assumed constant at 650 °C, while pressure is varied between 2 and 3 GPa. Biotite-melt partition coefficients near unity are predicted. The dotted lines are an uncertainty envelope (68% confidence) propagated from Eq. (5).

(Figs. 7 and 8). The self-limiting nature of N loss should favor the drawdown of atmospheric N (pN2) on the billion-year time scale due to the retention of N in minerals, either in the crust or mantle. Only small decreases the fraction of N lost to the arc translate into large increases in the flux of nitrogen to the mantle, if the fraction lost to the arc is near one, as implied by the fluid-mobile nature of N at high concentration (Fig. 8). For example, the mantle return flux is doubled if slab loss of N decreases from 99 to 98%. Indeed, surface-interior exchange models allow for the possibility that pN2 has decreased since the Archean (Johnson and Goldblatt, 2018). Paleoconstraints for pN2, however, suggest little change (Marty et al., 2013), and perhaps some thickening (Som et al., 2016) on the billon-year time scale. Moreover, peridotiteassociated diamonds show little evidence for subducted N over geologic time, and mass flux models argue for little exchange of N between the atmosphere and mantle when isotopes are considered (Cartigny et al., 1998; Labidi et al., 2020).

If little N has been sequestered from the atmosphere over Earth's history, then much of the N subducted must be liberated from slabs. For context, the current subduction flux estimates of N suggest the full mass of atmospheric N has been subducted over 4 billion years (Goldblatt et al., 2009; Halama et al. 2014). Previous experimental work highlights the importance of oxidizing and warm slabs in promoting the concentration of N into fluids from minerals (Förster et al., 2019; Jackson et al., 2021). Our finding that N reactivity with silicate depends on concentration only further emphasizes the potential importance oxidizing and warm slabs in maintaining Earth's atmosphere since the Archean.

#### 5. Conclusions

We find that the partitioning of N between silicate phases (melts and K-bearing minerals) and fluids depends on N concentration under *PTX* conditions applicable to slab dehydration. Natural systems contain highly variable concentrations of N, and experiments that constrain N partitioning between silicate and fluid phases tend to be completed at high N concentrations. We suggest that N concentration be taken into consideration when modeling N behavior in natural systems and when interpreting experimental data, in light of our experimental observations.

# **Declaration of Competing Interest**

The authors declare that they have no known competing financial interests or personal relationships that could have appeared to influence the work reported in this paper.

#### Acknowledgements

We acknowledge the support of Tim Rose in electron microprobe analysis, Ben Andrews for discussions and methods development, and Istiak Hossain for help with Raman analyses. CRMJ was supported by Tulane Startup and NSF Grants EAR 1725315 and CAREER 2144842. EC acknowledges support from the Lyda Hill Foundation. Constructive reviews by Yuan Li, Ananya Mallik, and an anonymous reviewer all helped to improve the content and clarity of the manuscript. We additionally thank Ralf Halama for editorial handling and comments.

# Appendix A. Supplementary material

We include in the Supplementary Information a comparison of  $K\alpha$  peak centers for N in tobelite and silicon nitride (Supplementary Figure 1) and a comparison of residual nitrogen concentrations with analytical totals (Supplementary Figure 2). We also include a section that details our estimate for N detection limits in this study. We also append data tables to the Supplementary Material as follows: Supplementary Table 1 reports starting compositions, Supplementary Table 2 reports run conditions, Supplementary Table 3 reports melt analyses, Supplementary Table 4 reports biotite analyses, Supplementary Table 5 reports pyroxene analyses, and Supplementary Table 6 reports Raman spectra. Supplementary material to this article can be found online at htt ps://doi.org/10.1016/j.gca.2023.05.017.

#### References

- Bebout, G.E., Fogel, M.L., 1992. Nitrogen-isotope compositions of metasedimentary rocks in the Catalina Schist, California - implications for metamorphic devolatilization history. Geochim. Cosmochim. Acta 56, 2839–2849.
- Beran, A., Armstrong, J., Rossman, G.R., 1992. Infrared and electron microprobe analysis of ammonium ions in hyalophane feldspar. Eur. J. Mineral. 4, 847–850.
- Bos, A., Duit, W., Vandereerden, A.M.J., Jansen, J.B.H., 1988. Nitrogen storage in biotite: an experimental study of the ammonium and potassium partitioning between 1Mphlogopite and vapor at 2 kb. Geochim. Cosmochim. Acta 52, 1275–1283.
- Botcharnikov, R.E., Behrens, H., Holtz, F., 2006. Solubility and speciation of C-O-H fluids in andesitic melt at  $T=1100-1300\,^{\circ}\text{C}$  and P=200 and 500 MPa. Chem. Geol. 229, 125–143.
- Boulliung, J., Füri, E., Dalou, C., Tissandier, L., Zimmermann, L., Marrocchi, Y., 2020. Oxygen fugacity and melt composition controls on nitrogen solubility in silicate melts. Geochim. Cosmochim. Acta 284, 120–133.
- Busigny, V., Cartigny, P., Philippot, P., Ader, M., Javoy, M., 2003. Massive recycling of nitrogen and other fluid-mobile elements (K, Rb, Cs, H) in a cold slab environment: Evidence from HP to UHP oceanic metasediments of the Schistes Lustres nappe (Western Alps, Europe). Earth Planet. Sci. Lett. 215, 27–42.
- Busigny, V., Cartigny, P., Philippot, P., 2011. Nitrogen isotopes in ophiolitic metagabbros: a re-evaluation of modern nitrogen fluxes in subduction zones and implication for the early earth atmosphere. Geochim. Cosmochim. Acta 75, 7502, 751.
- Carroll, M.R., Stolper, E.M., 1993. Noble gas solubilities in silicate melts and glasses: New experimental results for argon and the relationship between solubility and ionic porosity. Geochim. Cosmochim. Acta 57, 5039–5051.
- Cartigny, P., Harris, J.W., Javoy, M., 1998. Eclogitic diamond formation at Jwaneng: No room for a recycled component. Science 280, 1421–1424.
- Dalou, C., Hirschmann, M.M., Jacobsen, S.D., Le Losq, C., 2019. Raman spectroscopy study of COHN speciation in reduced basaltic glasses: Implications for reduced planetary mantles. Geochim. Cosmochim. Acta 265, 32–47.
- Fischer, T.P., Hilton, D.R., Zimmer, M.M., Shaw, A.M., Sharp, Z.D., Walker, J.A., 2002. Subduction and recycling of nitrogen along the Central American margin. Science 297, 1154–1157.
- Förster, M.W., Foley, S.F., Alard, O., Buhre, S., 2019. Partitioning of nitrogen during melting and recycling in subduction zones and the evolution of atmospheric nitrogen. Chem. Geol. 525, 334–342.
- Gao, Z., Yang, Y.-N., Yang, S.-Y., Li, Y., 2022. Experimental determination of N<sub>2</sub> solubility in silicate melts and implications for N<sub>2</sub>–Ar–CO<sub>2</sub> fractionation in magmas. Geochim. Cosmochim. Acta 326, 17–40.
- Goldblatt, C., Claire, M.W., Lenton, T.M., Matthews, A.J., Watson, A.J., Zahnle, K.J., 2009. Nitrogen-enhanced greenhouse warming on early earth. Nat. Geosci. 2, 891–896.
- Grewal, D.S., Dasgupta, R., Farnell, A., 2020. The speciation of carbon, nitrogen, and water in magma oceans and its effect on volatile partitioning between major reservoirs of the solar system rocky bodies. Geochim. Cosmochim. Acta 280, 281–301
- Halama, R., Bebout, G.E., John, T., Scambelluri, M., 2014. Nitrogen recycling in subducted mantle rocks and implications for the global nitrogen cycle. Int. J. Earth Sci. 103, 2081–2099.

- Halama, R., Bebout, G.E., Marschall, H.R., John, T., 2017. Fluid-induced breakdown of white mica controls nitrogen transfer during fluid–rock interaction in subduction zones. Int. Geol. Rev. 59, 702–720.
- Heber, V.S., Brooker, R.A., Kelley, S.P., Wood, B.J., 2007. Crystal-melt partitioning of noble gases (helium, neon, argon, krypton, and xenon) for olivine and clinopyroxene. Geochim. Cosmochim. Acta 71, 1041–1061.
- Hilton, D.R., Fischer, T.P., Marty, B., 2002. Noble gases and volatile recycling at subduction zones. In: Donald, P., Porcelli, D.P., Ballentine, C.P., Wieler, R. (Eds.), Noble Gases in Geochemistry and Cosmochemistry. Mineralogical Society of America and Geochemical Society, Washington, DC, USA, pp. 319–370.
- Huang, W.L., Wyllie, P., 1973. Melting relations of muscovite-granite to 35 kbar as a model for fusion of metamorphosed subducted oceanic sediments. Contrib. Miner. Petrol. 42, 1–14.
- Jackson, C.R.M., Parman, S.W., Kelley, S.P., Cooper, R.F., 2013. Constraints on light noble gas partitioning at the conditions of spinel-peridotite melting. Earth Planet. Sci. Lett. 384, 178–187.
- Jackson, C.R.M., Parman, S.W., Kelley, S.P., Cooper, R.F., 2015. Light noble gas dissolution into ring structure-bearing materials and lattice influences on noble gas recycling. Geochim. Cosmochim. Acta 159, 1–15.
- Jackson, C.R.M., Cottrell, E., Andrews, B., 2021. Warm and oxidizing slabs limit ingassing efficiency of nitrogen to the mantle. Earth Planet. Sci. Lett. 553, 116615.
- Jarrard, R.D., 2003. Subduction fluxes of water, carbon dioxide, chlorine, and potassium. Geochem. Geophys. Geosyst. 4, 8905.
- Johnson, B.W., Goldblatt, C., 2018. EarthN: A new earth system nitrogen model. Geochem. Geophys. Geosyst. 19, 2516–2542.
- Johnson, M.C., Plank, T., 2000. Dehydration and melting experiments constrain the fate of subducted sediments. Geochem. Geophys. Geosyst. 1 (12).
- Labidi, J., 2022. The origin of nitrogen in Earth's mantle: Constraints from basalts  $^{15}\text{N}/^{14}\text{N}$  and  $\text{N}_2/^3\text{He}$  ratios. Chem. Geol. 597, 120780.
- Labidi, J., Barry, P.H., Bekaert, D.V., Broadley, M.W., Marty, B., Giunta, T., Warr, O., Lollar, B.S., Fischer, T.P., Avice, G., 2020. Hydrothermal <sup>15</sup>N<sup>15</sup>N abundances constrain the origins of mantle nitrogen. Nature 580, 367–371.
- Labidi, J., Young, E.D., Fischer, T.P., Barry, P.H., Ballentine, C.J., de Moor, J.M., 2021. Recycling of nitrogen and light noble gases in the Central American subduction zone: Constraints from <sup>15</sup>N<sup>15</sup>N. Earth Planet. Sci. Lett. 571, 117112.
- Lambert, I., Wyllie, P., 1972. Melting of gabbro (quartz eclogite) with excess water to 35 kilobars, with geological applications. J. Geol. 80, 693–708.
- Li, L., Bebout, G.E., 2005. Carbon and nitrogen geochemistry of sediments in the Central American convergent margin: Insights regarding subduction input fluxes, diagenesis, and paleoproductivity. J. Geophys. Res.-Solid Earth 110, B11.
- Li, L., Bebout, G.E., Idleman, B.D., 2007. Nitrogen concentration and delta 8<sup>15</sup>N of altered oceanic crust obtained on ODP Legs 129 and 185: Insights into alterationrelated nitrogen enrichment and the nitrogen subduction budget. Geochim. Cosmochim. Acta 71, 2344–2360.
- Li, Y., Huang, R., Wiedenbeck, M., Keppler, H., 2015. Nitrogen distribution between aqueous fluids and silicate melts. Earth Planet. Sci. Lett. 411, 218–228.
- Li, Y., Keppler, H., 2014. Nitrogen speciation in mantle and crustal fluids. Geochim. Cosmochim. Acta 129, 13–32.
- Li, Y., Wiedenbeck, M., Shcheka, S., Keppler, H., 2013. Nitrogen solubility in upper mantle minerals. Earth Planet. Sci. Lett. 377, 311–323.
- Libourel, G., Marty, B., Humbert, F., 2003. Nitrogen solubility in basaltic melt. Part i. Effect of oxygen fugacity. Geochim. Cosmochim. Acta 67, 4123–4135.
- Luginbühl, S.M., 2015. Phase relations, compositions and trace element partitioning of solid and mobile phases in the hydrous MORB system at 2-3 GPa. Doctoral Thesis, ETH Zurich.
- Mallik, A., Li, Y., Wiedenbeck, M., 2018. Nitrogen evolution within the earth's atmosphere-mantle system assessed by recycling in subduction zones. Earth Planet. Sci. Lett. 482, 556–566.
- Marty, B., Zimmermann, L., 1999. Volatiles (He, C, N, Ar) in mid-ocean ridge basalts: Assessment of shallow-level fractionation and characterization of source composition. Geochim. Cosmochim. Acta 63, 3619–3633.
- Marty, B., Zimmermann, L., Pujol, M., Burgess, R., Philippot, P., 2013. Nitrogen isotopic composition and density of the Archean atmosphere. Science 342, 101–104.
- Mikhail, S., Sverjensky, D.A., 2014. Nitrogen speciation in upper mantle fluids and the origin of Earth's nitrogen-rich atmosphere. Nat. Geosci. 7, 816–819.
- Mingram, B., Bräuer, K., 2001. Ammonium concentration and nitrogen isotope composition in metasedimentary rocks from different tectonometamorphic units of the European Variscan Belt. Geochim. Cosmochim. Acta 65, 273–287.
- Mitchell, E.C., Fischer, T.P., Hilton, D.R., Hauri, E.H., Shaw, A.M., de Moor, J.M., Sharp, Z.D., Kazahaya, K., 2010. Nitrogen sources and recycling at subduction zones: Insights from the Izu-Bonin-Mariana arc. Geochem. Geophys. Geosyst. 11.
- Mosenfelder, J.L., Von Der Handt, A., Füri, E., Dalou, C., Hervig, R.L., Rossman, G.R., Hirschmann, M.M., 2019. Nitrogen incorporation in silicates and metals: Results from SIMS, EPMA, FTIR, and laser-extraction mass spectrometry. Am. Mineral. 104, 31–46.
- Mysen, B.O., Fogel, M.L., 2010. Nitrogen and hydrogen isotope compositions and solubility in silicate melts in equilibrium with reduced (N + H)-bearing fluids at high pressure and temperature: Effects of melt structure. Am. Mineral. 95, 987–999.
- Mysen, B.O., Yamashita, S., Chertkova, N., 2008. Solubility and solution mechanisms of NOH volatiles in silicate melts at high pressure and temperature-amine groups and hydrogen fugacity. Am. Mineral. 93, 1760–1770.
- Plank, T., Langmuir, C.H., 1998. The chemical composition of subducting sediment and its consequences for the crust and mantle. Chem. Geol. 145, 325–394.
- Plessen, B., Harlov, D.E., Henry, D., Guidotti, C.V., 2010. Ammonium loss and nitrogen isotopic fractionation in biotite as a function of metamorphic grade in metapelites from western Maine, USA. Geochim. Cosmochim. Acta 74, 4759–4771.

- Poli, S., Schmidt, M.W., 2002. Petrology of subducted slabs. Annu. Rev. Earth Planet. Sci.
- Pöter, B., Gottschalk, M., Heinrich, W., 2004. Experimental determination of the ammonium partitioning among muscovite, k-feldspar, and aqueous chloride solutions. Lithos 74, 67–90.
- Roskosz, M., Mysen, B.O., Cody, G.D., 2006. Dual speciation of nitrogen in silicate melts at high pressure and temperature: An experimental study. Geochim. Cosmochim. Acta 70, 2902–2918.
- Sadofsky, S.J., Bebout, G.E., 2000. Ammonium partitioning and nitrogen-isotope fractionation among coexisting micas during high-temperature fluid-rock interactions: Examples from the New England Appalachians. Geochim. Cosmochim. Acta 64, 2835–2849.
- Sano, Y., Takahata, N., Nishio, Y., Marty, B., 1998. Nitrogen recycling in subduction zones. Geophys. Res. Lett. 25, 2289–2292.
- Schmidt, C., Watenphul, A., 2010. Ammonium in aqueous fluids to  $600\,^{\circ}$ C, 1.3 GPa: A spectroscopic study on the effects on fluid properties, silica solubility, and k-feldspar to muscovite reactions. Geochim. Cosmochim. Acta 74, 6852–6866.
- Som, S.M., Buick, R., Hagadorn, J.W., Blake, T.S., Perreault, J.M., Harnmeijer, J.P., Catling, D.C., 2016. Earth's air pressure 2.7 billion years ago constrained to less than half of modern levels. Nat. Geosci. 9, 448–451.
- Stolper, E., 1982. The speciation of water in silicate melts. Geochim. Cosmochim. Acta  $46,\,2609{-}2620.$
- Stüeken, E.E., Kipp, M.A., Koehler, M.C., Buick, R., 2016. The evolution of Earth's biogeochemical nitrogen cycle. Earth Sci. Rev. 160, 220–239.
- Syracuse, E.M., van Keken, P.E., Abers, G.A., 2010. The global range of subduction zone thermal models. Phys. Earth Planet. In. 183, 73–90.
- van Keken, P.E., Hacker, B.R., Syracuse, E.M., Abers, G.A., 2011. Subduction factory: 4.

  Depth-dependent flux of H<sub>2</sub>O from subducting slabs worldwide. J. Geophys. Res.Solid Earth 116.